

# Assembly of Dy<sub>60</sub> and Dy<sub>30</sub> cage-shaped nanoclusters

Zhi-Rong Luo<sup>1,3</sup>, Hai-Ling Wang<sup>1,3</sup>, Zhong-Hong Zhu<sup>1</sup> <sup>✉</sup>, Tong Liu<sup>1</sup>, Xiong-Feng Ma<sup>1</sup> <sup>✉</sup>, Hui-Feng Wang<sup>1</sup>, Hua-Hong Zou<sup>1</sup> <sup>✉</sup> & Fu-Pei Liang<sup>1,2</sup> <sup>✉</sup>

Rapid kinetics, complex and diverse reaction intermediates, and difficult screening make the study of assembly mechanisms of high-nuclearity lanthanide clusters challenging. Here, we synthesize a double-cage dysprosium cluster [Dy<sub>60</sub>(H<sub>2</sub>L<sup>1</sup>)<sub>24</sub>(OAc)<sub>71</sub>(O)<sub>5</sub>(OH)<sub>3</sub>(H<sub>2</sub>O)<sub>27</sub>]-6H<sub>2</sub>O-6CH<sub>3</sub>OH-7CH<sub>3</sub>CN (**Dy<sub>60</sub>**) by using a multidentate chelate-coordinated diacylhydrazone ligand. Two **Dy<sub>30</sub>** cages are included in the **Dy<sub>60</sub>** structure, which are connected via an OAc<sup>-</sup> moiety. The core of **Dy<sub>60</sub>** is composed of 8 triangular Dy<sub>3</sub> and 12-fold linear Dy<sub>3</sub> units. We further change the alkali added in the reaction system and successfully obtain a single cage-shaped cluster [Dy<sub>30</sub>(H<sub>2</sub>L<sup>1</sup>)<sub>12</sub>(OAc)<sub>36</sub>(OH)<sub>4</sub>(H<sub>2</sub>O)<sub>12</sub>]-2OH-10H<sub>2</sub>O-12CH<sub>3</sub>OH-13CH<sub>3</sub>CN (**Dy<sub>30</sub>**) with a perfect spherical cavity, which could be considered an intermediate in **Dy<sub>60</sub>** formation. Time-dependent, high-resolution electrospray ionization mass spectrometry (HRESI-MS) is used to track the formation of **Dy<sub>60</sub>**. A possible self-assembly mechanism is proposed. We track the formation of **Dy<sub>30</sub>** and the six intermediate fragments are screened.

<sup>1</sup>State Key Laboratory for Chemistry and Molecular Engineering of Medicinal Resources, School of Chemistry and Pharmacy of Guangxi Normal University, Guilin 541004, China. <sup>2</sup>Guangxi Key Laboratory of Electrochemical and Magnetochemical Functional Materials, College of Chemistry and Bioengineering, Guilin University of Technology, Guilin 541004, China. <sup>3</sup>These authors contributed equally: Zhi-Rong Luo, Hai-Ling Wang. ✉email: [18317725515@163.com](mailto:18317725515@163.com); [maxiongfeng1992@163.com](mailto:maxiongfeng1992@163.com); [gxnuchem@foxmail.com](mailto:gxnuchem@foxmail.com); [fliangoffice@yahoo.com](mailto:fliangoffice@yahoo.com)

Over the past few decades, the design and synthesis of high-nuclearity lanthanide clusters with complex structures and interesting properties has been extremely active (Supplementary Table 1)<sup>1–5</sup>. To date, a variety of high-nuclearity lanthanide clusters (e.g., **Gd**<sub>140</sub>, **Ln**<sub>104</sub>, **Dy**<sub>76</sub>, **Dy**<sub>72</sub>, **Er**<sub>60</sub>, **Gd**<sub>60</sub>, and **Ln**<sub>48</sub>) have been designed and synthesized, and their magnetic, optical, and catalytic applications have been successfully extended<sup>1–12</sup>. Although considerable progress has been made in the synthesis and performance expansion of high-nuclearity lanthanide clusters, there are still only two relatively mature synthetic strategies, namely ligand-controlled hydrolysis and anionic template strategies<sup>1,2</sup>. In ligand-controlled hydrolysis, Ln(III) ion is initially combined with water and allowed to further participate in hydrolysis to obtain a template precursor, such as linear {Ln<sub>2</sub>(μ<sub>2</sub>-OH)}, triangular {Ln<sub>3</sub>(μ<sub>3</sub>-OH)} or {Ln<sub>3</sub>(μ<sub>3</sub>-OH)<sub>2</sub>}, tetrahedral {Ln<sub>4</sub>(μ<sub>3</sub>-OH)<sub>4</sub>}, trigonal bipyramidal {Ln<sub>5</sub>(μ<sub>3</sub>-OH)<sub>6</sub>}, square pyramidal {Ln<sub>5</sub>(μ<sub>3</sub>-OH)<sub>4</sub>(μ<sub>4</sub>-O)}, and octahedral {Ln<sub>6</sub>(μ<sub>3</sub>-OH)<sub>8</sub>(μ<sub>6</sub>-O)} precursors<sup>1</sup>. In 2014, Long and colleagues<sup>7</sup> hydrolyzed Ln(ClO<sub>4</sub>)<sub>3</sub> in the presence of acetate to obtain Ln-exclusive high-nuclearity cluster **Ln**<sub>104</sub> containing 24 independent units [Ln<sub>5</sub>(μ<sub>3</sub>-OH)<sub>4</sub>(μ<sub>4</sub>-O)]<sup>9+</sup>. Zheng and colleagues<sup>9</sup> finally synthesized the tubular dysprosium cluster **Dy**<sub>72</sub> by controlling the hydrolysis of Dy(III) ions via *N*-methyl-diethanolamine. The ligand-controlled hydrolysis process is mainly determined by the hydrolysis of Ln(III) ions<sup>1,2</sup>. During hydrolysis, different shapes of hydroxyl intermediate templates are generated to further aggregate and construct high-nuclearity lanthanide clusters<sup>1</sup>. Therefore, the synthesis of high-nuclearity lanthanide clusters via ligand-controlled hydrolysis is sensitive to the selection of reaction raw materials and reaction conditions, and different hydroxy intermediate templates are easily generated during the reaction to make the reaction disordered<sup>1,8</sup>. As such, tracking the reaction process and exploring its self-assembly mechanism have become difficult tasks. In the anionic template strategy, the formation of high-nuclearity lanthanide clusters is hindered by the mutual exclusion of positive charges between Ln(III) ions. Therefore, introducing a small volume of anion as a reaction building block is an effective strategy for solving the abovementioned problems<sup>1,2</sup>. In comparison with a single anion template, multiple anions or mixed different anions as templates can disperse the positive charge of Ln(III) ions in the cluster and are conducive to the synthesis of high-nuclearity lanthanide clusters; such anions further act as a negative charge to balance the positive charge in the cluster<sup>1,8</sup>. In 2015, Zhao and colleagues<sup>13</sup> formed eight CO<sub>3</sub><sup>2-</sup> templates via in-situ ligand decomposition and obtained a cage-shaped cluster **Ln**<sub>60</sub>. Thereafter, Tong and colleagues<sup>14</sup> induced the synthesis of two Gd(III) clusters **Gd**<sub>38</sub> and **Gd**<sub>48</sub> by using Cl<sup>-</sup> and NO<sub>3</sub><sup>-</sup> templates. Song and colleagues<sup>11</sup> used a combination of OAc<sup>-</sup> and CO<sub>3</sub><sup>2-</sup> mixed templates to synthesize nanocluster **Gd**<sub>60</sub>. In 2019, Bu and colleagues<sup>8</sup> used mixed anions Cl<sup>-</sup> and CO<sub>3</sub><sup>2-</sup> as templates to induce the formation of basic construction units [Dy<sub>3</sub>(μ<sub>3</sub>-OH)<sub>4</sub>] and [Dy<sub>5</sub>(μ<sub>4</sub>-O)(μ<sub>3</sub>-OH)<sub>8</sub>], and synthesized **Dy**<sub>76</sub>. When synthesizing high-nuclearity lanthanide clusters through the anionic template strategy, the reaction is complicated due to the diversity of anion selection and the uncontrollability of the template<sup>1,2</sup>. Therefore, selecting the appropriate method and means to track self-assembly is difficult.

In the design and synthesis of high-nuclearity lanthanide clusters, multidentate chelating ligands can rapidly bind and stabilize Ln(III) ions, making their self-assembly regular<sup>15–19</sup>. The selection of suitable multidentate chelating ligands is instrumental for studies on the assembly mechanism of high-nuclearity lanthanide clusters<sup>20,21</sup>. The acylhydrazone ligands with strong chelating ability, multiple coordination modes, and easily changing coordination configurations have made progress in the synthesis of low-nuclear lanthanide clusters<sup>15–17</sup>; however, their use in the

design and synthesis of giant lanthanide clusters is rare<sup>18,19</sup>. In 2016, we synthesized the largest lanthanide wheel-like cluster **Gd**<sub>18</sub> at the time by using acylhydrazone ligands<sup>18</sup>. We used different lanthanide metal salts and obtained **Gd**<sub>11</sub> with a high magneto-caloric effect under the same reaction conditions<sup>19</sup>. In the hydrothermal/solvothermal “black box” system under certain temperature and pressure conditions, the temperature and pressure in a closed system make the collision between reaction species confusing. Thus, the exploration of the assembly mechanism of coordination molecular clusters is slow<sup>20–35</sup>. Although complex, progress has been made in polyoxometalates<sup>22–25,36,37</sup>, coordination supramolecular systems<sup>38,39</sup>, coordination molecular cages<sup>26,40–45</sup>, 3d metal-ion clusters<sup>30–33</sup>, and so on<sup>46,47</sup>. High-valence Ln(III) ions usually have complex coordination configurations, rich and diverse coordination modes, and coordination balls that are prone to distortion<sup>20,21,48–50</sup>. Such drawbacks lead to the formation of several types of assembly methods in the synthesis of high-nuclearity lanthanide clusters, such as multi-template induction and stepwise assembly<sup>20,21,48–50</sup>. Given that various assembly methods exist, the formation process of high-nuclearity lanthanide clusters is confusing and exploring the assembly mechanism is difficult<sup>20,21,48–50</sup>. Therefore, studies on the assembly mechanism of lanthanide clusters are limited<sup>20,21,48–51</sup>. In 2018, Long and colleagues<sup>51</sup> used high-resolution electrospray ionization mass spectrometry (HRESI-MS) to guide the assembly and synthesis of the wheel-like **Eu**<sub>24</sub>**Ti**<sub>8</sub> cluster. We initially used HRESI-MS to track the assembly of Dy-exclusive coordination cluster **Dy**<sub>3</sub> and proposed its assembly mechanism<sup>20</sup>. In 2019, we used HRESI-MS to track the stepwise assembly of **Dy**<sub>10</sub> with multiple relaxation behavior<sup>21</sup>. Subsequently, we traced the assembly of a nanocluster **Dy**<sub>12</sub> composed of four vertices sharing Dy<sub>4</sub>(μ-OH)<sub>4</sub> via HRESI-MS. The relationship between stepwise and template assembly in the formation of high-nuclearity lanthanide clusters was described<sup>48</sup>. Finally, we tracked the competitive assembly process of mixed ligands and in-situ Schiff base replacement in the formation of lanthanide clusters via HRESI-MS<sup>49,50</sup>.

Here we synthesize the Dy-exclusive double-cage-shaped cluster **Dy**<sub>60</sub> under solvothermal conditions by using diacylhydrazone ligands with multidentate chelating coordination (Supplementary Figs. 1 and 2). Tetrabutyl ammonium hydroxide (Bu<sub>4</sub>NOH) in the reaction of **Dy**<sub>60</sub> synthesis is changed to LiOH, whereby the stable intermediate **Dy**<sub>30</sub> is obtained under the same reaction conditions. The stoichiometric reaction of **Dy**<sub>30</sub>, Bu<sub>4</sub>NOH, and Dy(OAc)<sub>3</sub>·4H<sub>2</sub>O under solvothermal conditions resulted in the high-yield synthesis of the cluster **Dy**<sub>60</sub> (Supplementary Fig. 2). Time-dependent HRESI-MS track the formation of **Dy**<sub>60</sub>. We proposed the **Dy**<sub>60</sub> possible assembly mechanism as follows: H<sub>6</sub>L<sup>1</sup> → DyL<sup>1</sup> → Dy<sub>2</sub>L<sup>1</sup> → Dy<sub>3</sub>L<sup>1</sup> → Dy<sub>4</sub>L<sup>1</sup> → Dy<sub>5</sub>(L<sup>1</sup>)<sub>2</sub> → Dy<sub>30</sub>(L<sup>1</sup>)<sub>12</sub> → Dy<sub>60</sub>(L<sup>1</sup>)<sub>24</sub>. We used the same method to track the formation of **Dy**<sub>30</sub> and further verify the assembly mechanism of **Dy**<sub>60</sub>. A possible assembly mechanism of **Dy**<sub>30</sub> is as follows: H<sub>6</sub>L<sup>1</sup> → DyL<sup>1</sup> → Dy<sub>2</sub>L<sup>1</sup> → Dy<sub>3</sub>L<sup>1</sup> → Dy<sub>4</sub>L<sup>1</sup> → Dy<sub>5</sub>(L<sup>1</sup>)<sub>2</sub> → Dy<sub>30</sub>(L<sup>1</sup>)<sub>12</sub>.

## Results and discussion

**Crystal structural analysis.** The nanocluster **Dy**<sub>60</sub> was synthesized using Dy(OAc)<sub>3</sub>·4H<sub>2</sub>O, (*N*<sup>3</sup>*E,N*<sup>5</sup>*E*)-4-hydroxy-*N*<sup>3</sup>,*N*<sup>5</sup>-bis(2-hydroxybenzylidene)-1*H*-pyrazole-3,5-dicarbohydrazide (H<sub>6</sub>L<sup>1</sup>), and tetrabutyl ammonium hydroxide (Bu<sub>4</sub>NOH) in the presence of mixed solvent (CH<sub>3</sub>OH:CH<sub>3</sub>CN = 1 : 1, 1.6 mL) under solvothermal conditions for 2 days at 80 °C. Single-crystal X-ray diffraction pattern revealed that nanocluster **Dy**<sub>60</sub> crystallized in the triclinic *P*-1 space group (Supplementary Table 2) containing 60 Dy(III) ions, 24 (H<sub>2</sub>L<sup>1</sup>)<sup>4-</sup> ligands, 5 μ<sub>3</sub>-O<sup>2-</sup>, 3 OH<sup>-</sup>, one bridged μ<sub>2</sub>-OAc<sup>-</sup>, 70 OAc<sup>-</sup>, and 27 H<sub>2</sub>O molecules (Fig. 1a).

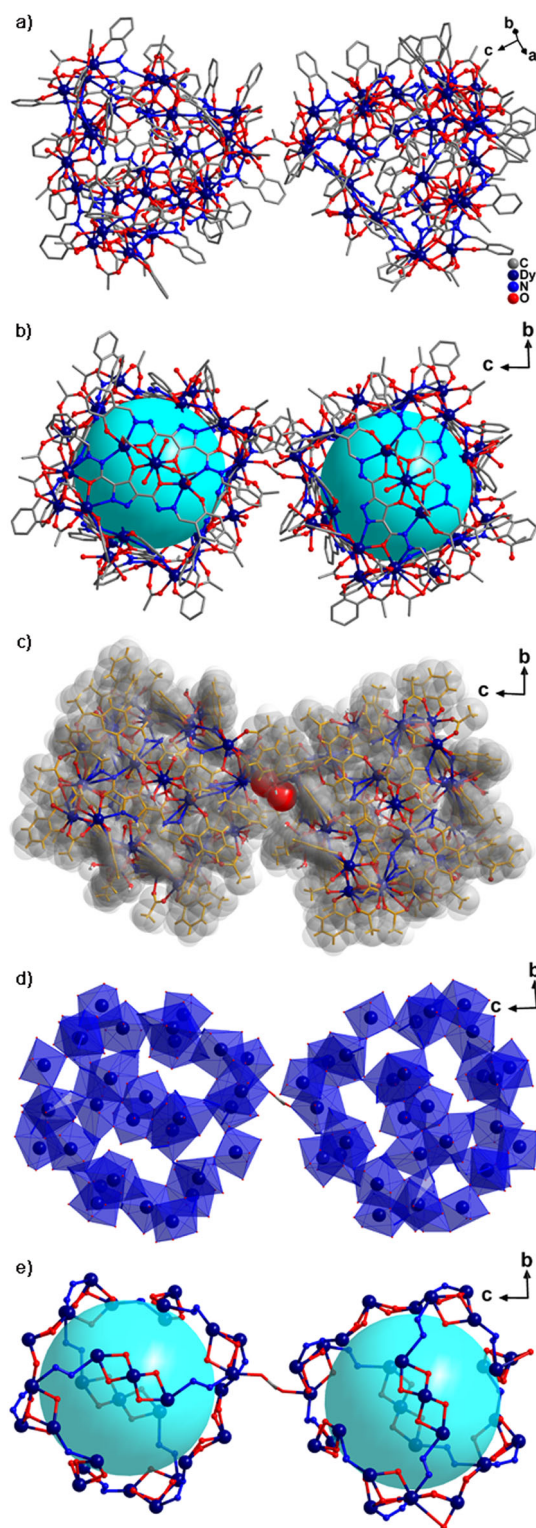


**Fig. 1** Crystal structure of **Dy<sub>60</sub>**. **a** Molecular structure of the cage-shaped **Dy<sub>60</sub>**. **b** Illustration of **Dy<sub>60</sub>**. **c** Space-filling mode of **Dy<sub>60</sub>**, which exhibited all ligands protected the two main cores. **d** Polyhedron of Dy(III) ions in Dy...Dy cage. **e** Cage mode in Dy/O/N core.

The size of nanocluster **Dy<sub>60</sub>** was 5.2 nm × 2.7 nm and the diameter of every cavity was 1.5 nm (Dy<sub>13</sub>...Dy<sub>21</sub>) (Fig. 1b). The volume of the above spherical cavity is 2.4 nm<sup>3</sup>. The periphery of the Dy/O/N core of **Dy<sub>60</sub>** was covered by 24 (H<sub>2</sub>L)<sup>4-</sup> ligands forming the organic ligand structure that protected the Dy/O/N

core of **Dy<sub>60</sub>** in the periphery (Fig. 1c, d). In this nano-sized Dy(III) cluster, the main core of **Dy<sub>60</sub>** was composed of eight triangular Dy<sub>3</sub> and 12-fold linear Dy<sub>3</sub> units. In the Dy/O/N core of **Dy<sub>30</sub>**, each Dy(III) ion in the four triangular lattices Dy<sub>3</sub> was connected by a folding linear Dy<sub>3</sub> through the -N-N- bridging on the ligand. The two cage-shaped **Dy<sub>30</sub>** was formed **Dy<sub>60</sub>** by bridging the Dy(III) ions of the two triangular lattices by one μ<sub>2</sub>-OAc<sup>-</sup> (Fig. 1e). In the Dy/O core of **Dy<sub>60</sub>**, the bond distances of Dy...Dy in triangular lattices Dy<sub>3</sub> were within the limits of 3.805–3.939 Å and the bond distances of Dy...Dy were within the limits of 3.707–3.836 Å in the folding linear Dy<sub>3</sub> (Supplementary Fig. 3a). The ligand in **Dy<sub>60</sub>** showed one coordination mode in the structure: μ<sub>5</sub>-η<sup>1</sup>:η<sup>1</sup>:η<sup>2</sup>:η<sup>2</sup>:η<sup>1</sup>:η<sup>1</sup>:η<sup>2</sup>:η<sup>1</sup>:η<sup>1</sup> (Supplementary Fig. 3b). OAc<sup>-</sup> is mainly used for short-bridged ligands during **Dy<sub>60</sub>** formation. OAc<sup>-</sup> can coordinate with Dy(III) ions to make them saturated and bridge several adjacent Dy(III) ions in the cluster, thereby ensuring the stability of the cage high-core cluster **Dy<sub>60</sub>**. A structural figure of **Dy<sub>60</sub>** with probability ellipsoids is given in Supplementary Fig. 4.

High nuclear lanthanide clusters usually form ring-type (**Gd<sub>140</sub>**)<sup>6</sup>, hamburger-type<sup>8</sup>, disordered-type<sup>52</sup>, and ellipsoid configuration<sup>53</sup> structures through simple anion ligands (Supplementary Table 1). However, the formation of cage-shaped clusters is rare, in which the high nuclear caged lanthanide cluster **Er<sub>60</sub>** is a sodalite caged structure composed of 24 [Er<sub>4</sub>(μ<sub>3</sub>-OH)<sub>4</sub>]<sup>8+</sup> cubanes by vertex sharing<sup>10</sup>. Cage-shaped dysprosium high-nuclearity clusters, such as **Dy<sub>17</sub>**, **Dy<sub>24</sub>**, **Dy<sub>26</sub>**, **Dy<sub>27</sub>**, and **Dy<sub>104</sub>** have been reported<sup>54–57</sup>. **Dy<sub>104</sub>** is composed of four single cage-shaped **Dy<sub>26</sub>** bridged by ligands.

The nanocluster **Dy<sub>60</sub>** can be interpreted as two **Dy<sub>30</sub>** connected by one bridged OAc<sup>-</sup>, thereby providing a new structural model for the lanthanide clusters. The single cage-shaped nanocluster **Dy<sub>30</sub>** should be synthesized to verify the rationality of connecting two nanocluster **Dy<sub>30</sub>** with one OAc<sup>-</sup> bridge. We attempted to block the formation of the final state by shortening the reaction time via the same method for the synthesis of **Dy<sub>60</sub>**. However, we did not obtain the crystal of **Dy<sub>30</sub>** under the same experimental conditions. A single cage-shaped nanocluster **Dy<sub>30</sub>** was successfully obtained by replacing Bu<sub>4</sub>NOH with LiOH during nanocluster **Dy<sub>60</sub>** synthesis. We also successfully obtained the cluster **Dy<sub>60</sub>** by reacting **Dy<sub>30</sub>**, Bu<sub>4</sub>NOH, and Dy(OAc)<sub>3</sub>·4H<sub>2</sub>O under solvothermal conditions.

The nanocluster **Dy<sub>30</sub>** was determined via single-crystal X-ray diffraction. The nanocluster **Dy<sub>30</sub>** crystallized in the trigonal *P*-3c1 space group (Fig. 2a and Supplementary Table 2), which contained 30 Dy(III) ions, 12 (H<sub>2</sub>L)<sup>4-</sup> ligands, 4 OH<sup>-</sup>, 36 OAc<sup>-</sup>, 12 H<sub>2</sub>O, and 2 free OH<sup>-</sup>. The size of the nanocluster **Dy<sub>30</sub>** was 2.8 nm × 2.7 nm and the cavity diameter was 1.5 nm (Fig. 2b). The periphery of the Dy/O/N **Dy<sub>30</sub>** core was covered by 12 (H<sub>2</sub>L)<sup>4-</sup> ligands and 36 OAc<sup>-</sup>, forming the structure that enabled the organic ligands to protect the Dy/O/N core of **Dy<sub>30</sub>** (Fig. 2c, d). Each Dy(III) ion in the four triangular lattices Dy<sub>3</sub> was connected by a folding linear Dy<sub>3</sub> through -N-N- bridging on the ligand to form a **Dy<sub>30</sub>** core composed of four triangular Dy<sub>3</sub> and sixfold linear Dy<sub>3</sub> units (Fig. 2e). The Dy/O/N core of **Dy<sub>30</sub>** exhibited a spherical cage shape and differed from the octagonal-prismatic **Dy<sub>17</sub>**, capsule-shaped **Dy<sub>24</sub>**, ball-and-stick-shaped **Dy<sub>27</sub>**, and vertex angle cage-shaped **Dy<sub>26</sub>** (or **Dy<sub>104</sub>**) (Fig. 2e)<sup>54–57</sup>. In the core of **Dy<sub>30</sub>**, the bond distances of Dy...Dy were within the limits of 3.895–3.925 Å in the triangular lattice Dy<sub>3</sub>. The bond distances of Dy...Dy were within the limits of 3.774–3.812 Å in the folding linear Dy<sub>3</sub> (Supplementary Fig. 3c), and the bond distances of Dy...Dy between triangular lattice Dy<sub>3</sub> and folding linear Dy<sub>3</sub> were 5.654–5.717 Å. The ligand in the **Dy<sub>30</sub>** core showed one coordination mode in the structure: μ<sub>5</sub>-η<sup>1</sup>:η<sup>1</sup>:η<sup>2</sup>:η<sup>2</sup>:η<sup>1</sup>:η<sup>1</sup>:η<sup>2</sup>:η<sup>1</sup>:η<sup>1</sup> (Fig. 2f). Structural figure of **Dy<sub>30</sub>** with probability

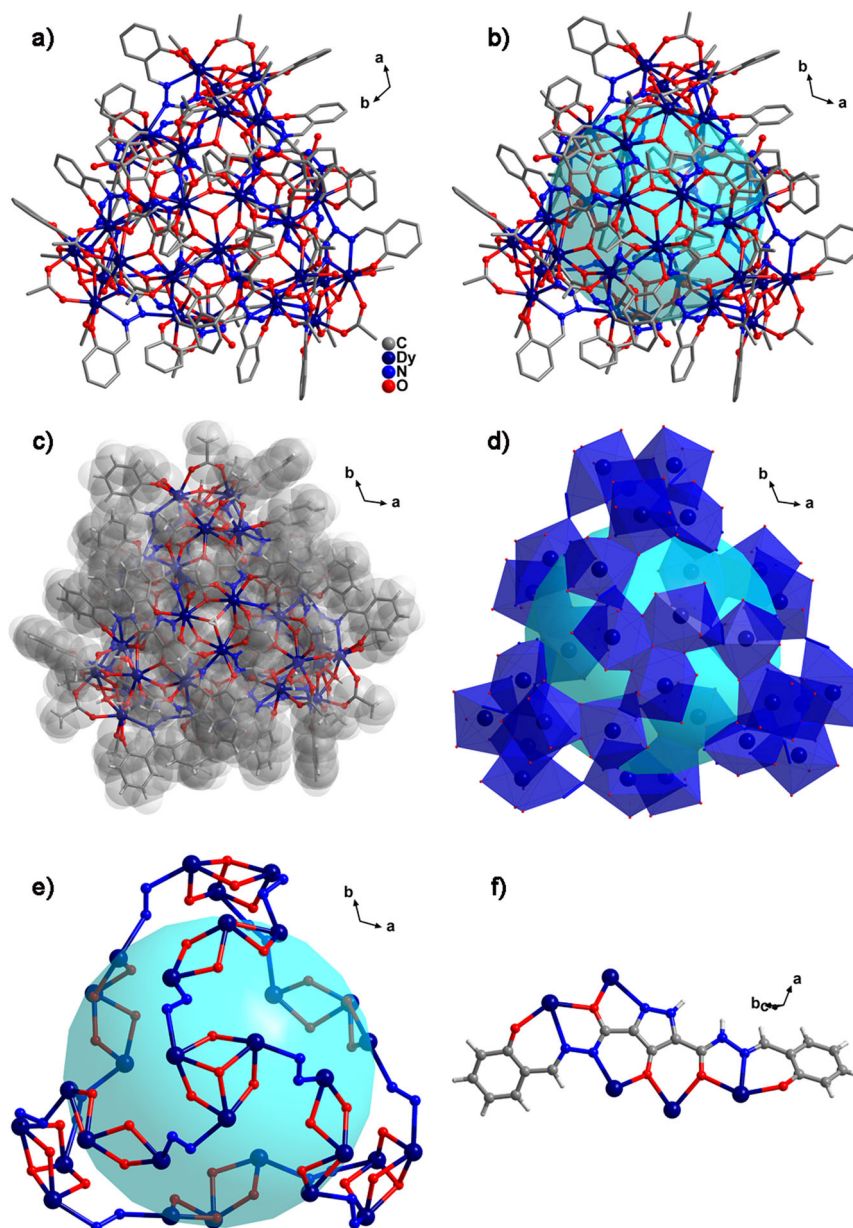


**Fig. 2** Crystal structure of  $\text{Dy}_{30}$ . **a** Molecular structure of cage-shaped  $\text{Dy}_{30}$ . **b** Illustration of  $\text{Dy}_{30}$ . **c** Space-filling mode of  $\text{Dy}_{30}$ . **d** Polyhedron of Dy(III) ions in Dy...Dy cage. **e** Cage mode in the Dy/O/N core. **f** Coordinated mode of  $\text{L}^1$ .

ellipsoids in Supplementary Fig. 5. The thermogravimetric analysis (TGA) curves of  $\text{Dy}_{60}$  and  $\text{Dy}_{30}$  are discussed in Supplementary Note 2 and shown in Supplementary Fig. 6. The phase purity of  $\text{Dy}_{60}$  and  $\text{Dy}_{30}$  was examined from their powder X-ray diffraction (PXRD) patterns (Supplementary Note 3 and Supplementary Fig. 7).

SQUEEZE calculations were performed to determine the electron counts per unit cells (Supplementary Note 1).

**Assembly mechanism analysis.** Coordination molecule clusters are usually synthesized under hydrothermal/solvothermal conditions at a certain temperature and pressure. Given the temperature and pressure, the tracking and exploration of the self-assembly mechanism were extremely difficult. The outermost electron orbitals of the metal center had clusters of coordination molecules of unpaired electrons and self-assembly was difficult to track via

nuclear magnetic resonance spectroscopy (NMR)<sup>48–51</sup>. In recent years, our group used HRESI-MS to track the formation of several lanthanide clusters and proposed their assembly mechanism. For example, the assembly mechanism of Dy-exclusive clusters  $\text{Dy}_3$ ,  $\text{Dy}_4$ ,  $\text{Dy}_{10}$ , and  $\text{Dy}_{12}$  was proposed<sup>20,21,48–50</sup>. On the basis of the above work, we used HRESI-MS to track the self-assembly of the double-cage-shaped dysprosium cluster  $\text{Dy}_{60}$  and its interphase  $\text{Dy}_{30}$ . The self-assembly of the coordination cage molecular cluster  $\text{Dy}_{60}$  and intermediate  $\text{Dy}_{30}$  was further inferred by analyzing the species of fragments existing in the solution in different time periods, the time-dependent intensity variation, and the abundance of fragments in the instrument. This work was the first to systematically study the self-assembly mechanism cage coordination molecular clusters. We set the specific time interval in the reaction to remove the same amount of solution from the reaction system, further diluting each equal amount of reaction solution with the same proportion of chromatographic methanol.

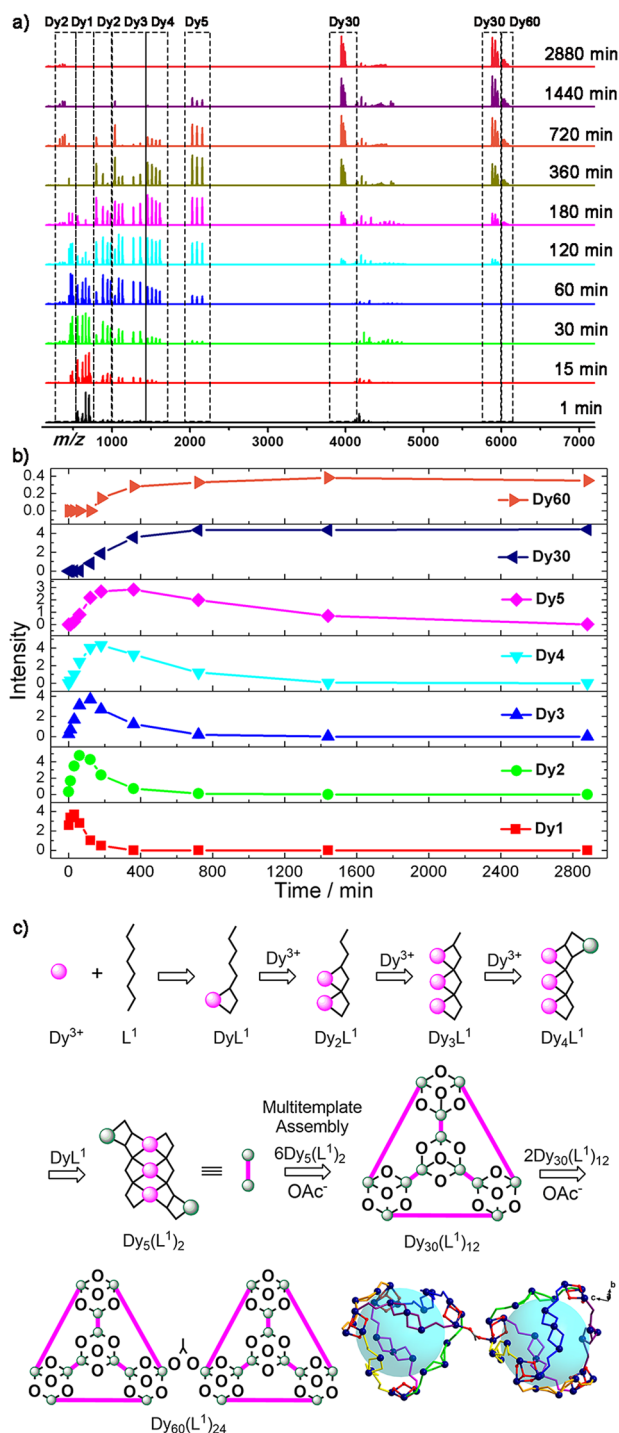


**Fig. 3** Assembly mechanism analysis of **Dy<sub>60</sub>**. **a** Time-dependent assembly of cage-shaped **Dy<sub>60</sub>** in cationic mode. **b** HRESI-MS spectra intensity–time profiles of the species in the assembly. **c** Possible assembly mechanism for **Dy<sub>60</sub>**.

Data on the anion and cationic modes were collected via HRESI-MS and analyzed.

The data collected in the cationic mode in different time periods of cluster **Dy<sub>60</sub>** formation are shown in Fig. 3a. We propose a plausible assembly mechanism, which is consistent with our data (Fig. 3b). The most reasonable assembly mechanism of **Dy<sub>60</sub>** is shown in Fig. 3c. The HRESI-MS data of **Dy<sub>60</sub>** assembly were analyzed and the results suggested that unit **Dy<sub>5</sub>** was obtained via step assembly. A cage-like **Dy<sub>30</sub>** was formed

via step-by-step and multi-template assembly, and the two molecules of **Dy<sub>30</sub>** were bridged by OAc<sup>-</sup> to obtain **Dy<sub>60</sub>**. Before heating (0–1 min), the monocyte **DyL<sup>1</sup>** (**Dy<sub>1</sub>**) was the main intensity ( $m/z = 558.07\text{--}758.18$ ). The molecular formula of the reaction system was  $[\text{Dy}(\text{H}_x\text{L}^1)(\text{OAc})_y(\text{solv.})]^+$  ( $x \leq 2$ ,  $y \leq 2$ ,  $x + y = 2$ ). After heating for 30 min, the content of **DyL<sup>1</sup>** in the reaction system decreased gradually for 3 h. The low-strength **Dy<sub>2</sub>L<sup>1</sup>** (**Dy<sub>2</sub>**) fragment ( $m/z = 447.54\text{--}491.56$ ,  $882.07\text{--}983.12$ ) appeared in the period of 0–30 min. The molecular formula of the binuclear fragment was  $[\text{Dy}_2(\text{H}_x\text{L}^1)(\text{OAc})_y(\text{solv.})]^+$  ( $y \leq 2$ ,  $2 \leq x \leq 4$ ,  $x + y = 5$ ) or  $[\text{Dy}_2(\text{H}_x\text{L}^1)(\text{OAc})_y(\text{solv.})]^{2+}$  ( $y \leq 2$ ,  $2 \leq x \leq 4$ ,  $x + y = 4$ ). With prolonged reaction time, the intensity of **Dy<sub>2</sub>L<sup>1</sup>** was the highest level in 1 h, thereby indicating that the **Dy<sub>2</sub>L<sup>1</sup>** fragment was obtained by chelating **Dy<sup>3+</sup>** ion under solvothermal conditions. **Dy<sub>2</sub>L<sup>1</sup>** fragments decreased gradually from 1 h to 12 h. With the further progress of self-assembly, the molecular ion peak of the fragment **Dy<sub>3</sub>L<sup>1</sup>** (**Dy<sub>3</sub>**) appeared in the range of  $m/z = 1085.97\text{--}1362.15$  positions. The general formula of the fragments  $[\text{Dy}_3(\text{H}_x\text{L}^1)(\text{OAc})_y(\text{solv.})]^+$  ( $y \leq 4$ ,  $x \leq 2$ ,  $x + y = 8$ ) was obtained by fitting. At a reaction time of 2 h, the **Dy<sub>3</sub>L<sup>1</sup>** fragment reached the highest intensity. The intensity of the reaction continued to decrease gradually and disappeared after 24 h. As such, the binuclear fragment **Dy<sub>2</sub>L<sup>1</sup>** continued to capture **Dy<sup>3+</sup>** ions to form **Dy<sub>3</sub>L<sup>1</sup>** fragments during this time period. At 15 min of the reaction, the molecular ion peaks produced by **Dy<sub>4</sub>L<sup>1</sup>** (**Dy<sub>4</sub>**) fragments appeared in the range of  $m/z = 798.53$  and  $1457.96\text{--}1613.08$ , and the general formulas were obtained by fitting  $[\text{Dy}_4(\text{H}_x\text{L}^1)(\text{OAc})_y(\text{solv.})]^+$  ( $y \leq 4$ ,  $x \leq 2$ ,  $x + y = 8$ ). The intensity of the above **Dy<sub>4</sub>L<sup>1</sup>** fragments increased with prolonged reaction time and reached the highest intensity at 3 h, indicating that the **Dy<sub>4</sub>L<sup>1</sup>** fragments were continuously produced in the reaction system. At a reaction time of 30 min, the molecular ion peak of **Dy<sub>5</sub>(L<sup>1</sup>)<sub>2</sub>** (**Dy<sub>5</sub>**) appeared in the range of  $m/z = 2031.03\text{--}2160.10$  and the general formulas of  $[\text{Dy}_5(\text{H}_2\text{L}^1)_2(\text{OAc})_y(\text{O})_z(\text{solv.})]^+$  ( $z \leq 1$ ,  $5 \leq y \leq 6$ ,  $y + z = 6$ ) were obtained by fitting. The intensity of the above **Dy<sub>5</sub>(L<sup>1</sup>)<sub>2</sub>** fragments reached its highest level in 6 h and decreased rapidly thereafter. Thus, a large number of **Dy<sub>5</sub>(L<sup>1</sup>)<sub>2</sub>** fragments was used for the next assembly. After 1 h, a small amount of molecular ion peak **Dy<sub>30</sub>(L<sup>1</sup>)<sub>12</sub>** (**Dy<sub>30</sub>**) appeared in the range of  $m/z = 3900\text{--}6000$  and its molecular formula was  $[\text{Dy}_{30}(\text{H}_2\text{L}^1)_{12}(\text{OAc})_{35}(\text{OH})_4(\text{solv.})]^{3+}$  or  $[\text{Dy}_{30}(\text{H}_2\text{L}^1)_{12}(\text{OAc})_{35}(\text{OH})_3(\text{solv.})]^{4+}$ . With prolonged heating time, the intensity of **Dy<sub>30</sub>(L<sup>1</sup>)<sub>12</sub>** gradually increased to the highest level. The highest level was reached from 12 h, indicating that the multimolecular **Dy<sub>5</sub>(L<sup>1</sup>)<sub>2</sub>** fragment was assembled by template to form the **Dy<sub>30</sub>(L<sup>1</sup>)<sub>12</sub>** fragment. With continuous reaction for 3 h, the molecular ion peak of **Dy<sub>60</sub>(L<sup>1</sup>)<sub>24</sub>** (**Dy<sub>60</sub>**) appeared in the range of  $m/z = 6000\text{--}6100$  and their molecular formulas were  $[\text{Dy}_{60}(\text{H}_2\text{L}^1)_{24}(\text{OAc})_{71}(\text{OH})_6(\text{solv.})]^{2+}$ . With prolonged time, the abundance of the above fragment increased gradually, but the overall strength of the fragments was not high. The structure of the final cluster was compared, and the fragment was a **Dy<sub>60</sub>(L<sup>1</sup>)<sub>24</sub>** fragment frame formed by two **Dy<sub>30</sub>(L<sup>1</sup>)<sub>12</sub>** fragments bridged by an OAc<sup>-</sup> bridge. However, the abundance of the fragment was not high under the condition of HRESI-MS test, because the OAc<sup>-</sup> connection was unstable. Analysis of the fragment abundance and changing trend in cationic mode indicated that the cage coordination molecular cluster **Dy<sub>60</sub>** formed via step-by-step and multi-template assembly (Supplementary Table 3 and Supplementary Fig. 8). Combined with structural analysis, the possible assembly mechanism is as follows:  $\text{H}_x\text{L}^1 \rightarrow \text{DyL}^1 \rightarrow \text{Dy}_2\text{L}^1 \rightarrow \text{Dy}_3\text{L}^1 \rightarrow \text{Dy}_4\text{L}^1 \rightarrow \text{Dy}_5(\text{L}^1)_2 \rightarrow \text{Dy}_{30}(\text{L}^1)_{12} \rightarrow \text{Dy}_{60}(\text{L}^1)_{24}$  (Fig. 3c). This is a possible assembly mechanism indicated by the time-dependent HRESI-MS tracking cluster **Dy<sub>60</sub>** formation process. The main frame peak appeared at the  $m/z = 399.98$  positions in the negative mode and the molecular fragment was

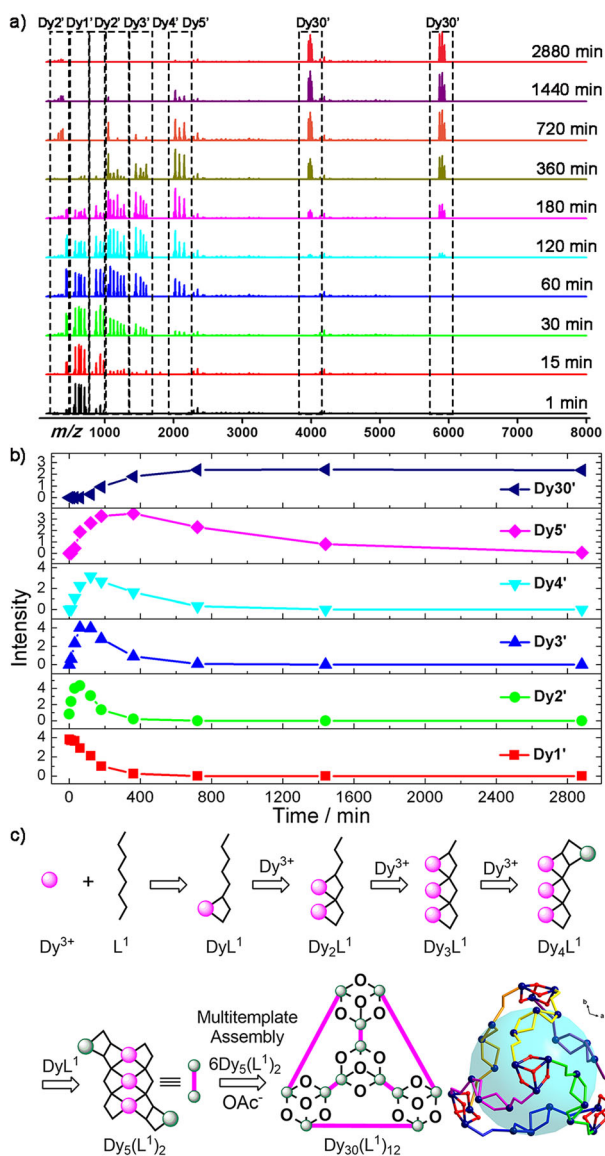


**Fig. 4** Assembly mechanism analysis of  $\text{Dy}_{30}$ . **a** Time-dependent HRESI-MS of cage-shaped  $\text{Dy}_{30}$  in cationic mode. **b** HRESI-MS spectra intensity-time profiles of the species. **c** Possible assembly mechanism of  $\text{Dy}_{30}$ .

$[\text{Dy}(\text{OAc})_4]^-$  (calc. 399.98) by fitting (Supplementary Figs. 9 and 10). To further verify the above assembly mechanism, we have tried to volatilize the reaction solution at different time periods, but have not obtained the structure of the intermediate. As for the fragments  $\text{Dy}_1 \sim \text{Dy}_5$  are intermediates of  $\text{Dy}_{60}$  formation process, the above intermediates are very unstable in solution and have high Gibbs free energy, so we think it is difficult for them to remain in the reaction solution for a long time and crystallize.

A cage-shaped coordination molecule cluster  $\text{Dy}_{30}$  was successfully obtained by replacing  $\text{Bu}_4\text{NOH}$  in the reaction system with  $\text{LiOH}$  and reacting under the same conditions to verify the accuracy of  $\text{Dy}_{60}$  assembly mechanism. The  $\text{Dy}_{30}$  structure described above verified the mechanism of  $\text{Dy}_{60}$  assembly. We also used HRESI-MS to track the  $\text{Dy}_{30}$  reaction. As shown in Fig. 4a, the variation trend of the time dependence of the molecular ion peak intensity of each component was plotted in Fig. 4b. The most reasonable assembly mechanism of the single

cage-shaped coordination molecular cluster  $\text{Dy}_{30}$  was estimated in Fig. 4c. The HRESI-MS data for the analysis of the assembly of the cage-shaped coordination molecule cluster  $\text{Dy}_{30}$  were similar to that of  $\text{Dy}_{60}$  and the self-assembly process was first subjected to step-by-step assembly to form a construction unit. Finally, the final cage-shaped coordination molecular cluster  $\text{Dy}_{30}$  was formed via one-step multi-template assembly. The reaction system was the main strength ( $m/z = 576.07\text{--}752.18$ ) and the molecular formulas were  $[\text{Dy}(\text{H}_x\text{L}^1)(\text{CH}_3\text{O})_y(\text{OH})_z(\text{solv.})]^+$  ( $x \leq 2$ ,  $y \leq 1$ ,  $z \leq 1$ ,  $x + y + z = 2$ ). The intensity of  $\text{DyL}^1$  in the further reaction system gradually decreased after 15 min of the reaction. The  $\text{Dy}_2\text{L}^1$  ( $\text{Dy}_2'$ ) fragment ( $m/z = 440.54\text{--}454.58$ ,  $887.07\text{--}987.12$ ) with low intensity appeared for the time period from 0 min to 15 min. The molecular formula of the  $\text{Dy}_2\text{L}^1$  fragments obtained by fitting were  $[\text{Dy}_2(\text{HL}^1)(\text{OAc})_y(\text{CH}_3\text{O})_z(\text{solv.})]^+$  ( $y \leq 2$ ,  $z \leq 1$ ,  $y + z = 2$ ) or  $[\text{Dy}_2(\text{H}_x\text{L}^1)(\text{OAc})_y(\text{solv.})]^{2+}$  ( $y \leq 2$ ,  $3 \leq x \leq 4$ ,  $x + y = 5$ ). During the reaction, the abundance of the  $\text{Dy}_2\text{L}^1$  fragment reached the highest at 30 min and gradually decreased from 30 min and almost disappeared after 6 h. The reaction continued and the molecular ion peak of  $\text{Dy}_3\text{L}^1$  ( $\text{Dy}_3'$ ) appeared in the range of  $m/z = 1085.97\text{--}1362.15$ , and the molecular formula of the fragment peaks was determined by fitting to  $[\text{Dy}_3(\text{H}_x\text{L}^1)(\text{OAc})_y(\text{solv.})]^+$  ( $y \leq 4$ ,  $x \leq 2$ ,  $x + y = 8$ ). At 1 h of reaction time, the fragment  $\text{Dy}_3\text{L}^1$  reached the highest intensity and the intensity of the reaction decreased gradually and disappeared after 6 h. A certain amount of  $\text{Dy}_4\text{L}^1$  ( $\text{Dy}_4'$ ) fragment was present in the solution after 15 min and its molecular ion peaks appeared in the range of  $m/z = 1453.97\text{--}1604.08$ . The molecular formulas of  $[\text{Dy}_4(\text{H}_2\text{L}^1)(\text{OAc})_y(\text{O})_z(\text{solv.})]^+$  ( $y \leq 6$ ,  $z \leq 1$ ,  $y + z = 6$ ) were obtained by fitting. The intensity of the  $\text{Dy}_4\text{L}^1$  fragments was increased at the end of the reaction and reached the highest intensity in 2 h. The molecular ion peaks of  $\text{Dy}_5(\text{L}^1)_2$

( $\text{Dy}_5'$ ) appeared in the range of  $m/z = 2026.03\text{--}2156.10$  and the molecular formulas of  $[\text{Dy}_5(\text{H}_2\text{L}^1)_2(\text{OAc})_y(\text{O})_z(\text{solv.})]^+$  ( $z \leq 1$ ,  $5 \leq y \leq 6$ ,  $y + z = 6$ ) were obtained by fitting. The intensity of the  $\text{Dy}_5(\text{L}^1)_2$  fragments peaked in 3 h. The  $\text{Dy}_5(\text{L}^1)_2$  fragment was rapidly involved in the next reaction. From 2 h, a molecular ion peak of  $\text{Dy}_{30}(\text{L}^1)_{12}$  ( $\text{Dy}_{30}$ ) appeared in  $m/z = 3900\text{--}6000$  and the molecular formulas of  $[\text{Dy}_{30}(\text{H}_2\text{L}^1)_{12}(\text{OAc})_{35}(\text{OH})_4(\text{solv.})]^{3+}$  or  $[\text{Dy}_{30}(\text{H}_2\text{L}^1)_{12}(\text{OAc})_{35}(\text{OH})_3(\text{solv.})]^{4+}$  were obtained by fitting. With prolonged heating time, the intensity of  $\text{Dy}_{30}(\text{L}^1)_{12}$  gradually increased and peaked, starting from 12 h to the highest. The segments  $\text{Dy}_5(\text{L}^1)_2$  formed  $\text{Dy}_{30}(\text{L}^1)_{12}$  fragments by template assembly during this time period (Supplementary Table 4 and Supplementary Fig. 11). With prolonged treatment, the  $\text{Dy}_{60}(\text{L}^1)_{24}$  fragment frameworks did not exhibit a high  $m/z$  range, indicating that  $\text{LiOH}$  added under these reaction conditions blocked the reaction; thus, stable intermediate segments  $\text{Dy}_{30}(\text{L}^1)_{12}$  were obtained. In conclusion, the assembly mechanism of the cage-shaped coordination molecular cluster  $\text{Dy}_{30}$  was found by analyzing the type of the fragment in the cation mode and its changing tendency as follows:  $\text{H}_6\text{L}^1 \rightarrow \text{DyL}^1 \rightarrow \text{Dy}_2\text{L}^1 \rightarrow \text{Dy}_3\text{L}^1 \rightarrow \text{Dy}_4\text{L}^1 \rightarrow \text{Dy}_5(\text{L}^1)_2 \rightarrow \text{Dy}_{30}(\text{L}^1)_{12}$  (Fig. 4c). This is a possible assembly mechanism proposed by time-dependent HRESI-MS tracking cluster  $\text{Dy}_{30}$  formation process. No molecular ion peak fragment with cluster nuclei  $>5$  was found in the reaction system, so we speculate that  $\text{Dy}_{30}$  may be formed by  $\text{Dy}_5(\text{L}^1)_2$  undergoing template assembly. The main frame peak appeared at the  $m/z = 399.98$  position in the negative mode and the molecular fragment was  $[\text{Dy}(\text{OAc})_4]^-$  (calc. 399.98) by fitting (Supplementary Figs. 12 and 13). The above results demonstrated the self-assembly mechanism of the maximum double-cage-shaped  $\text{Dy}_{60}$ . We also used HRESI-MS to verify the stability of all complexes in methanol;  $\text{Dy}_{30}$  is stable in the solution, which is in good agreement with the time-dependent process. Further, for  $\text{Dy}_{60}$  cluster, it does exist mainly as  $\text{Dy}_{30}$  fragments in the solution, but

there is also some fragment peak of the main frame **Dy**<sub>60</sub> (Supplementary Figs. 14 and 15).

The direct-current magnetic susceptibilities of **Dy**<sub>30</sub> and **Dy**<sub>60</sub> were tested from 300 K to 2 K under a 1000 Oe field (Supplementary Fig. 16). At 300 K, the  $\chi_m T$ -values were 421.88 and 842.576 cm<sup>3</sup> K mol<sup>-1</sup> for **Dy**<sub>30</sub> and **Dy**<sub>60</sub>, respectively, which were closed to the isolated values for 30 and 60 Dy(III) ions (<sup>6</sup>H<sub>15/2</sub>, *g* = 4/3). Upon cooling, the  $\chi_m T$ -values were marginally decreased up to ca. 100 K before going through shallow minima around 50 K. As the temperature decreased,  $\chi_m T$  decreased to 190.39 and 325.77 cm<sup>3</sup> K mol<sup>-1</sup> at 2 K for **Dy**<sub>30</sub> and **Dy**<sub>60</sub>.  $\chi_m^{-1}$  vs. *T* data above 100 K were analyzed using Curie–Weiss law and the obtained Curie constants (*C*) were 431.03 and 854.70 cm<sup>3</sup> K mol<sup>-1</sup>. The Weiss constants ( $\theta$ ) were -7.70 K and -5.13 K (Supplementary Fig. 17)<sup>8</sup>. The  $\chi_m T$  was rapidly decreasing in the low-temperature region probably attributed to thermal depopulation in Stark sublevels together with their different magnetic interactions. This decrease is mainly due to the thermal depopulation of the excited *m<sub>J</sub>* states of Dy(III) and/or the magnetic interactions.

The isothermal magnetization (*M*) of **Dy**<sub>30</sub> and **Dy**<sub>60</sub> were measured at different temperatures (Supplementary Fig. 18)<sup>8</sup>. The magnetization of **Dy**<sub>30</sub> was saturation for at 50 kOe and it reaches a maximum of 104.01 *N<sub>μB</sub>* at 50 kOe measured at 2 K. However, the absence of saturation for the magnetization of **Dy**<sub>60</sub> even at 50 kOe and it reaches a maximum of 206.82 *N<sub>μB</sub>* at 50 kOe measured at 2 K. We study their slow magnetic relaxation behaviors and the dynamic magnetic susceptibility of temperature dependence of **Dy**<sub>30</sub> and **Dy**<sub>60</sub>. The temperature-dependent  $\chi'$  and  $\chi''$  ac susceptibilities of **Dy**<sub>30</sub> and **Dy**<sub>60</sub> were measured from 2 to 12 K under 0 Oe at 1, 10, 499, 700, and 999 Hz, respectively (Supplementary Fig. 19). Magnetic tests showed that both **Dy**<sub>30</sub> and **Dy**<sub>60</sub> exhibited significant single-molecule magnet behavior. For further understanding of the relaxation process of **Dy**<sub>30</sub> and **Dy**<sub>60</sub>, Cole–Cole diagrams derived from frequency-dependent ac susceptibilities were drawn (Supplementary Figs. 20 and 21). The Cole–Cole plots followed a single relaxation Debye model, which affords the fitting parameters  $\tau$  (relaxation time) and  $\alpha$  (which determines the width of the distribution of relaxation times). The ln( $\tau$ /s) vs. *T*<sup>-1</sup> curves for **Dy**<sub>30</sub> and **Dy**<sub>60</sub> (Supplementary Figs. 19d and 20d) were also plotted from these fitting results. The temperature-dependent relaxation time was analyzed by assuming a thermally activated process following the Arrhenius law ( $\tau = \tau_0 \exp(U_{\text{eff}}/k_B T)$ ). In the low temperature, we applied an Orbach relaxation process ( $\tau^{-1} = \tau_0^{-1} \exp(-U_{\text{eff}}/k_B T)$ ). After performing Orbach fitting on **Dy**<sub>30</sub> and **Dy**<sub>60</sub>, we got their *U<sub>eff</sub>* = 11.15 K and 15.93 K,  $\tau_0 = 7.27 \times 10^{-6}$  s and  $1.66 \times 10^{-6}$  s, respectively. In addition, we considered the Orbach and Raman processes ( $\tau^{-1} = \tau_0^{-1} \exp(-U_{\text{eff}}/k_B T) + CT^n$ ) to fit **Dy**<sub>30</sub> and **Dy**<sub>60</sub> over the full temperature range, we got their *U<sub>eff</sub>* = 21.74 K and 20.14 K,  $\tau_0 = 2.88 \times 10^{-6}$  s and  $1.24 \times 10^{-6}$  s, respectively (Supplementary Figs. 10–21).

In summary, we synthesized the Dy-exclusive double-cage-shaped cluster **Dy**<sub>60</sub> under solvothermal conditions by using a diacylhydrazone ligand with multidentate coordination. **Dy**<sub>60</sub> was formed by two identical **Dy**<sub>30</sub>s through a  $\mu_2$ -OAc<sup>-</sup> bridge and its cluster core was composed of only two different types of Dy<sub>3</sub>, which were a triangular shape Dy<sub>3</sub> and a polygonal line type Dy<sub>3</sub>. We changed the base added in the reaction to obtain a single cage-shaped cluster **Dy**<sub>30</sub> with a spherical cavity. To the best of our knowledge, **Dy**<sub>30</sub> is currently the largest Dy-exclusive single cage-shaped cluster. HRESI-MS was used to track the formation of **Dy**<sub>60</sub>. Various intermediate fragments were screened and further combined with the changing trend of these intermediate fragments. We proposed the following possible self-assembly mechanism of **Dy**<sub>60</sub>:  $\text{H}_6\text{L}^1 \rightarrow \text{DyL}^1 \rightarrow \text{Dy}_2\text{L}^1 \rightarrow \text{Dy}_3\text{L}^1 \rightarrow$

$\text{Dy}_4\text{L}^1 \rightarrow \text{Dy}_5(\text{L}^1)_2 \rightarrow \text{Dy}_{30}(\text{L}^1)_{12} \rightarrow \text{Dy}_{60}(\text{L}^1)_{24}$ . Similarly, we tracked the formation of **Dy**<sub>30</sub> and proposed its possible assembly mechanism as follows:  $\text{H}_6\text{L}^1 \rightarrow \text{DyL}^1 \rightarrow \text{Dy}_2\text{L}^1 \rightarrow \text{Dy}_3\text{L}^1 \rightarrow \text{Dy}_4\text{L}^1 \rightarrow \text{Dy}_5(\text{L}^1)_2 \rightarrow \text{Dy}_{30}(\text{L}^1)_{12}$ . HRESI-MS did not find molecular ion peak fragments with cluster nuclei >5 in the reaction solution that formed **Dy**<sub>30</sub>, so we speculated that **Dy**<sub>30</sub> may be formed by Dy<sub>5</sub>(L<sup>1</sup>)<sub>2</sub> undergoing template assembly. The synthesis of the cluster **Dy**<sub>30</sub> and its assembly mechanism further verified the formation process of **Dy**<sub>60</sub>. We used crystallography and HRESI-MS combination technology to study the assembly mechanism of the Dy-exclusive double-cage-shaped cluster **Dy**<sub>60</sub> and its intermediate single cage-shaped cluster **Dy**<sub>30</sub>. To the best of our knowledge, this work is the first to use HRESI-MS for tracking the formation of cage-shaped Ln(III) clusters. This work provided a set of methods to study the formation tracking and assembly mechanism of high-nuclearity lanthanide clusters. It also lays the foundation for the further design and manipulation of high-nuclearity lanthanide clusters.

## Methods

**Materials and measurements.** All reagents were obtained from commercial sources and used without further purification. Elemental analyses for C, H, and N were performed on a vario MICRO cube. TGA analyses were conducted in a flow of nitrogen at a heating rate of 5 °C min<sup>-1</sup> using a NETZSCH TG 209 F3 (Supplementary Fig. 6). PXRD spectra were recorded on a D8 Advance (Bruker) diffractometer at 293 K (Cu-K $\alpha$ ). The samples were prepared by crushing crystals and the powder placed on a grooved aluminum plate. Diffraction patterns were recorded from 3° to 65° at a rate of 5° min<sup>-1</sup>. Calculated diffraction patterns of the compounds were generated with the Mercury software (Supplementary Fig. 7). Infrared spectra were recorded by transmission through KBr pellets containing ca. 0.5% of the complexes using a PE Spectrum FT-IR spectrometer (400–4000 cm<sup>-1</sup>).

**Single-crystal X-ray crystallography.** Diffraction data for these complexes were collected on a Bruker SMART CCD diffractometer (Cu-K $\alpha$  radiation and  $\lambda = 1.54184$  Å) in  $\Phi$  and  $\omega$  scan modes. The structures were solved by direct methods, followed by difference Fourier syntheses, and then refined by full-matrix least-squares techniques on *F*<sup>2</sup> using SHELXL<sup>58</sup>. All other non-hydrogen atoms were refined with anisotropic thermal parameters. Hydrogen atoms were placed at calculated positions and isotropically refined using a riding model. Supplementary Table S1 summarizes X-ray crystallographic data and refinement details for the complexes. Full details can be found in the CIF files provided in the Supplementary Information. The Cambridge Crystallographic Data Centre reference numbers are 1947876 (**Dy**<sub>30</sub>) and 1948703 (**Dy**<sub>60</sub>).

**HRESI-MS measurement.** HRESI-MS measurements were conducted at a capillary temperature of 275 °C. Aliquots of the solution were injected into the device at 0.3 mL h<sup>-1</sup>. The mass spectrometer used for the measurements was a Thermo-Exactive and the data were collected in positive and negative ion modes. The spectrometer was previously calibrated with the standard tune mix to give a precision of ca. 2 p.p.m. within the region of 200–7500 *m/z*. The capillary voltage was 50 V, the tube lens voltage was 150 V, and the skimmer voltage was 25 V.

**Crystal structure determination.** Because of the disorder of the free CH<sub>3</sub>OH and CH<sub>3</sub>CN molecules, parts of the CH<sub>3</sub>OH and CH<sub>3</sub>CN molecules are difficult to locate in the final structural refinement. The number of free molecules is further confirmed by elemental analyses and TGA analysis (Supplementary Fig. 4). Therefore, the chemical formula of complexes are found to be [Dy<sub>30</sub>(H<sub>2</sub>L<sup>1</sup>)<sub>12</sub>(OAc)<sub>36</sub>(OH)<sub>4</sub>(H<sub>2</sub>O)<sub>12</sub>·2OH·10H<sub>2</sub>O·12CH<sub>3</sub>OH·13CH<sub>3</sub>CN (**Dy**<sub>30</sub>) and [Dy<sub>60</sub>(H<sub>2</sub>L<sup>1</sup>)<sub>24</sub>(OAc)<sub>71</sub>(O)<sub>5</sub>(OH)<sub>3</sub>(H<sub>2</sub>O)<sub>27</sub>·6H<sub>2</sub>O·6CH<sub>3</sub>OH·7CH<sub>3</sub>CN (**Dy**<sub>60</sub>). Full details can be found in the CIF files.

**Synthesis of H<sub>6</sub>L<sup>1</sup>.** The synthetic route for H<sub>6</sub>L<sup>1</sup> is presented in Supplementary Fig. 1. Subsequently, the dimethyl 4-hydroxy-1H-pyrazole-3,5-dicarboxylate (2.00 g, 10 mmol) and N<sub>2</sub>H<sub>4</sub>·H<sub>2</sub>O (12.5 mL, 80%) was refluxed in MeOH (180 mL) at 80 °C for 12 h. The 2-hydroxybenzaldehyde (3.05 g, 25 mmol) were then added slowly and the reaction was kept at 80 °C for another 12 h. Upon cooling and filtering, light yellow solid of 4-hydroxy-*N,N'*-bis(2-hydroxybenzylidene)-1H-pyrazole-3,5-dicarbohydrazide (H<sub>6</sub>L<sup>1</sup>) was obtained with a yield of 90% (based on 4-hydroxy-1H-pyrazole-3,5-dicarboxylate). High resolution mass spectrometry (HRMS) (*m/z*): [M-H]<sup>-</sup> calcd. for C<sub>19</sub>H<sub>16</sub>N<sub>6</sub>O<sub>5</sub>, 408.1182; found, 407.1103. Elemental analysis (calcd., found for C<sub>19</sub>H<sub>16</sub>N<sub>6</sub>O<sub>5</sub>): C (55.88, 55.73), H (3.95, 3.88), N (20.58, 20.47). IR spectrum (cm<sup>-1</sup>): 3308 (m), 3142 (s), 3055 (s), 1662 (vs), 1619 (vs), 1586 (vs), 1546 (vs), 1489 (s), 1451 (s), 1370 (m), 1347 (m), 1321 (m), 1271 (vs), 1240 (s), 1196 (s), 1101 (w), 1035 (w), 956 (w), 946 (w), 871 (m),

796 (w), 653 (w), 615 (w), 566 (w), 532 (w), 479 (w), 449 (w).  $^1\text{H}$  NMR (400 MHz,  $\text{CDCl}_3$ ):  $\delta$  14.10 (s, 1H), 12.28 (s, 1H), 11.45 (s, 1H), 11.10 (s, 1H), 10.96 (s, 1H), 8.69 (d,  $J = 17.5$  Hz, 2H), 7.55 (s, 1H), 7.46 (s, 1H), 7.32–7.30 (m, 2H), 6.95–6.91 (m, 5H);  $^{13}\text{C}$  NMR (125 MHz,  $\text{CDCl}_3$ ):  $\delta$  159.2, 158.0, 157.9, 155.1, 149.5, 149.2, 143.6, 132.0, 131.8, 130.4, 129.9, 122.9, 119.8, 119.1, 116.9.

**The synthesis method of  $\text{Dy}_{60}$  and  $\text{Dy}_{30}$ .**  $\text{Dy}_{30}$ . A mixture of  $\text{Dy}(\text{OAc})_3 \cdot 4\text{H}_2\text{O}$  (0.5 mmol, 205.8 mg),  $\text{HL}^1$  ligand (0.1 mmol, 40.8 mg),  $\text{LiOH}$  (0.52 mmol, 12.4 mg), 1.6 mL mixed solvent ( $\text{CH}_3\text{OH} : \text{CH}_3\text{CN} = 1:1$ ) were stirred and sealed in a 20 cm-long Pyrex tube and heated at  $80^\circ\text{C}$  for 3 days, then it was taken out and slowly cooled to room temperature. In addition, square yellow crystals were observed (Supplementary Table 5). The yield was about 52% (based on ligand). Elemental analysis (calcd., found for  $\text{C}_{338}\text{H}_{389}\text{Dy}_{30}\text{N}_{85}\text{O}_{172}$ ): C (30.59, 30.43), H (2.95, 2.82), N (8.97, 8.78). IR (KBr,  $\text{cm}^{-1}$ ): 3007 (m), 1616 (s), 1546 (s), 1441 (w), 1305 (w), 1197 (m), 1034 (s), 891 (s), 761 (s), 648 (s), 534 (s).

$\text{Dy}_{60}$ : A mixture of  $\text{Dy}(\text{OAc})_3 \cdot 4\text{H}_2\text{O}$  (0.5 mmol, 205.8 mg),  $\text{HL}^1$  ligand (0.1 mmol, 40.8 mg), tetrabutyl ammonium hydroxide (120  $\mu\text{L}$ ), 1.6 mL mixed solvent ( $\text{CH}_3\text{OH} : \text{CH}_3\text{CN} = 1:1$ ) were stirred and sealed in a 20 cm-long Pyrex tube and heated at  $80^\circ\text{C}$  for 2 days, then it was taken out and slowly cooled to room temperature. In addition, square yellow crystals were observed (Supplementary Table 6). The yield was about 68% (based on ligand). Elemental analysis (calcd., found for  $\text{C}_{618}\text{H}_{615}\text{Dy}_{60}\text{N}_{151}\text{O}_{309}$ ): C (29.87, 29.71), H (2.49, 2.37), N (8.51, 8.39). IR (KBr,  $\text{cm}^{-1}$ ): 3008 (m), 1614 (s), 1544 (s), 1443 (w), 1307 (w), 1192 (m), 1036 (s), 893 (s), 761 (s), 646 (s), 537 (s).

## Data availability

All data used in this manuscript are available from the authors upon reasonable request. The X-ray crystallographic coordinates for structures reported in this article have been deposited at the Cambridge Crystallographic Data Centre (CCDC), under deposition number CCDC 1947876 ( $\text{Dy}_{30}$ ) and 1948703 ( $\text{Dy}_{60}$ ). These data can be obtained free of charge from The Cambridge Crystallographic Data Centre via hyperlink [http://www.ccdc.cam.ac.uk/data\\_request/cif](http://www.ccdc.cam.ac.uk/data_request/cif).

Received: 26 October 2019; Accepted: 6 February 2020;

Published online: 06 March 2020

## References

- Zheng, X.-Y. et al. Recent advances in the assembly of high-nuclearity lanthanide clusters. *Coord. Chem. Rev.* **378**, 222–236 (2019).
- Zheng, X.-Y. et al. High-nuclearity Lanthanide-containing clusters as potential molecular magnetic coolers. *Acc. Chem. Res.* **51**, 517–525 (2018).
- Zhang, P., Guo, Y.-N. & Tang, J. Recent advances in dysprosium-based single molecule magnets: structural overview and synthetic strategies. *Coord. Chem. Rev.* **257**, 1728–1763 (2013).
- Liu, J.-L. et al. Recent advances in the design of magnetic molecules for use as cryogenic magnetic coolants. *Coord. Chem. Rev.* **281**, 26–49 (2014).
- Jia, J.-H. et al. Luminescent single-molecule magnets based on lanthanides: design strategies, recent advances and magneto-luminescent studies. *Coord. Chem. Rev.* **378**, 365–381 (2019).
- Zheng, X.-Y. et al. A gigantic molecular wheel of  $\{\text{Gd}_{140}\}$ : a new member of the molecular wheel family. *J. Am. Chem. Soc.* **139**, 18178–18181 (2017).
- Peng, J.-B. et al. Beauty, symmetry, and magnetocaloric effect—four-shell keplerates with 104 lanthanide atoms. *J. Am. Chem. Soc.* **136**, 17938–17941 (2014).
- Li, X.-Y. et al. A giant  $\text{Dy}_{76}$  cluster: a new fused bi-nanopillar structural model in lanthanide clusters. *Angew. Chem. Int. Ed.* **58**, 10184–10188 (2019).
- Qin, L. et al. A “molecular water pipe”: a giant tubular cluster  $\{\text{Dy}_{72}\}$  exhibits fast proton transport and slow magnetic relaxation. *Adv. Mater.* **28**, 10772–10779 (2016).
- Kong, X.-J. et al. A chiral 60-metal sodalite cage featuring 24 vertex-sharing  $[\text{Er}_4(\mu_3\text{-OH})_4]$  cubanes. *J. Am. Chem. Soc.* **131**, 6918–6919 (2009).
- Luo, X.-M. et al. Exploring the performance improvement of magnetocaloric effect based Gd-exclusive cluster  $\text{Gd}_{60}$ . *J. Am. Chem. Soc.* **140**, 11219–11222 (2018).
- Wu, M. et al. Polymeric double-anion templated  $\text{Er}_{48}$  nanotubes. *Chem. Commun.* **50**, 1113–1115 (2014).
- Dong, J. et al. Ultrastrong alkali-resisting lanthanide-zeolites assembled by  $[\text{Ln}_{60}]$  nanocages. *J. Am. Chem. Soc.* **137**, 15988–15991 (2015).
- Guo, F. S. et al. Anion-templated assembly and magnetocaloric properties of a nanoscale  $\{\text{Gd}_{38}\}$  cage versus a  $\{\text{Gd}_{48}\}$  barrel. *Chem. Eur. J.* **19**, 14876–14885 (2013).
- Yang, Q. & Tang, J. Heterometallic grids: synthetic strategies and recent advances. *Dalton Trans.* **48**, 769–778 (2019).
- Wu, J. et al. Realization of toroidal magnetic moments in heterometallic 3d–4f metallocycles. *Chem. Commun.* **54**, 1065–1068 (2018).
- Li, X.-L. et al. End-to-end azido-pinned interlocking lanthanide squares. *Chem. Commun.* **53**, 3026–3029 (2017).
- Wang, K. et al. A single-stranded  $\{\text{Gd}_{18}\}$  nanowheel with a symmetric polydentate diacylhydrazone ligand. *Chem. Commun.* **52**, 8297–8300 (2016).
- Wang, K. et al. Diacylhydrazone-assembled  $\{\text{Ln}_{11}\}$  nanoclusters featuring a “double-boats conformation” topo-logy: synthesis, structures and magnetism. *Dalton Trans.* **47**, 2337–2343 (2018).
- Zhu, Z.-H. et al. A triangular  $\text{Dy}_3$  single-molecule toroic with high inversion energy barrier: magnetic properties and multiple-step assembly mechanism. *Inorg. Chem. Front.* **5**, 3155–3162 (2018).
- Wang, H.-L. et al. Tracking the stepwise formation of the dysprosium cluster ( $\text{Dy}_{10}$ ) with multiple relaxation behavior. *Inorg. Chem.* **58**, 9169–9174 (2019).
- Xuan, W. et al. Stereoselective assembly of gigantic chiral molybdenum blue wheels using lanthanide ions and amino acids. *J. Am. Chem. Soc.* **141**, 1242–1250 (2019).
- Christie, L. G. et al. Investigating the formation of giant  $\{\text{Pd}_{72}\}^{\text{Prop}}$  and  $\{\text{Pd}_{84}\}^{\text{Gly}}$  macrocycles using NMR, HPLC, and mass spectrometry. *J. Am. Chem. Soc.* **140**, 9379–9382 (2018).
- Cameron, J. M. et al. Investigating the transformations of polyoxoanions using mass spectrometry and molecular dynamics. *J. Am. Chem. Soc.* **138**, 8765–8773 (2016).
- Busche, C. et al. Design and fabrication of memory devices based on nanoscale polyoxometalate clusters. *Nature* **515**, 545–549 (2014).
- Sun, Q. F., Sato, S. & Fujita, M. An  $\text{M}_{18}\text{L}_{24}$  stellated cuboctahedron through post-stellation of an  $\text{M}_{12}\text{L}_{24}$  core. *Nat. Chem.* **4**, 330–333 (2012).
- Kitson, P. J. et al. Digitization of multistep organic synthesis in reactionware for on-demand pharmaceuticals. *Science* **359**, 314–319 (2018).
- Miras, H. N. et al. Unveiling the transient template in the self-assembly of a molecular oxide nanowheel. *Science* **327**, 72–74 (2010).
- Wang, Y. et al. Topology exploration in highly connected rare-earth metal-organic frameworks via continuous hindrance control. *J. Am. Chem. Soc.* **141**, 6967–6975 (2019).
- Guo, L.-Y. et al. Core-shell  $\{\text{Mn}_7(\text{Mn}, \text{Cd})_{12}\}$  assembled from core  $\{\text{Mn}_7\}$  disc. *J. Am. Chem. Soc.* **139**, 14033–14036 (2017).
- Deng, Y.-K. et al. Hierarchical assembly of a  $\{\text{Mn}^{\text{II}}_{15}\text{Mn}^{\text{III}}_4\}$  brucite disc: step-by-step formation and ferrimagnetism. *J. Am. Chem. Soc.* **138**, 1328–1334 (2016).
- Zheng, H. L. et al. Manipulating clusters by use of competing N,O-chelating ligands: a combined crystallographic, mass spectrometric, and DFT study. *Chem. Eur. J.* **24**, 7906–7912 (2018).
- Hu, Y. Q. et al. Tracking the formation of a polynuclear  $\text{Co}_{16}$  complex and its elimination and substitution reactions by mass spectroscopy and crystallography. *J. Am. Chem. Soc.* **135**, 7901–7908 (2013).
- Schröder, D. Applications of electrospray ionization mass spectrometry in mechanistic studies and catalysis research. *Acc. Chem. Res.* **45**, 1521–1532 (2012).
- Chen, X. M. & Tong, M. L. Solvothermal in situ metal/ligand reactions: a new bridge between coordination chemistry and organic synthetic chemistry. *Acc. Chem. Res.* **40**, 162–170 (2007).
- Pasparakis, G. et al. Controlled polymer synthesis—from biomimicry towards synthetic biology. *Chem. Soc. Rev.* **39**, 286–300 (2010).
- Ma, P., Hu, F., Wang, J. & Niu, J. Carboxylate covalently modified polyoxometalates: From synthesis, structural diversity to applications. *Coord. Chem. Rev.* **378**, 281–309 (2019).
- Chakrabarty, R., Mukherjee, P. S. & Stang, P. J. Supramolecular coordination: self-assembly of finite two- and three-dimensional ensembles. *Chem. Rev.* **111**, 6810–6918 (2011).
- Yu, G. C. et al. Antitumor activity of a unique polymer that incorporates a fluorescent self-assembled metallacycle. *J. Am. Chem. Soc.* **139**, 15940–15949 (2017).
- Wang, Q. M. et al. Role of anions associated with the formation and properties of silver clusters. *Acc. Chem. Res.* **48**, 1570–1579 (2015).
- Brown, C. J. et al. Supramolecular catalysis in metal–ligand cluster hosts. *Chem. Rev.* **115**, 3012–3035 (2015).
- Xu, F. et al. Correlating the magic numbers of inorganic nanomolecular assemblies with a  $\{\text{Pd}_{84}\}$  molecular-ring Rosetta Stone. *Proc. Natl Acad. Sci. USA.* **109**, 11609–11612 (2012).
- Kong, X. J. et al. Keeping the ball rolling: fullerene-like molecular clusters. *Acc. Chem. Res.* **43**, 201–209 (2010).
- Saha, M. L. et al. Photophysical properties of organoplatinum(II) compounds and derived self-assembled metallacycles and metallacages: fluorescence and its applications. *Acc. Chem. Res.* **49**, 2527–2539 (2016).
- Miras, H. N., Wilson, E. F. & Cronin, L. Unravelling the complexities of inorganic and supramolecular self-assembly in solution with electrospray and cryospray mass spectrometry. *Chem. Commun.* 1297–1311 (2009).
- Fujita, M., Powell, A. & Creutz, C. *From the Molecular to the Nanoscale: Synthesis, Structure, and Properties* 7 (Elsevier Ltd., Oxford, 2004).

47. Luo, Z. et al. Toward understanding the growth mechanism: tracing all stable intermediate species from reduction of Au(I)-thiolate complexes to evolution of Au<sub>25</sub> nanoclusters. *J. Am. Chem. Soc.* **136**, 10577–10580 (2014).
48. Ma, X.-F. et al. Formation of nanocluster {Dy<sub>12</sub>} containing Dy-exclusive vertex-sharing [Dy<sub>4</sub>(μ<sub>3</sub>-OH)<sub>4</sub>] cubanes via simultaneous multitemplate guided and step-by-step assembly. *Dalton Trans.* **48**, 11338–11344 (2019).
49. Wang, H.-L. et al. Step-by-step and competitive assembly of two Dy(III) single-molecule magnets with their performance tuned by Schiff base ligands. *Cryst. Growth Des.* **19**, 5369–5375 (2019).
50. Mo, K.-Q. et al. Tracking the multistep formation of Ln(III) complexes with in situ Schiff base exchange reaction and its highly selective sensing of dichloromethane. *Sci. Rep.* **9**, 12231–12237 (2019).
51. Zheng, H. et al. Assembly of a wheel-like Eu<sub>24</sub>Ti<sub>8</sub> cluster under the guidance of high-resolution electrospray ionization mass spectrometry. *Angew. Chem. Int. Ed.* **57**, 10976–10979 (2018).
52. Tian, H., Bao, S.-S. & Zheng, L.-M. Cyclic single-molecule magnets: from the odd-numbered heptanuclear to a dimer of heptanuclear dysprosium clusters. *Chem. Commun.* **52**, 2314–2317 (2016).
53. Zhou, Y. et al. Three giant lanthanide clusters Ln<sub>37</sub> (Ln = Gd, Tb, and Eu) featuring a double-cage structure. *Inorg. Chem.* **56**, 2037–2041 (2017).
54. Zhou, Y.-Y. et al. New family of octagonal-prismatic lanthanide coordination cages assembled from unique Ln<sub>17</sub> clusters and simple cliplike dicarboxylate ligands. *Inorg. Chem.* **55**, 2037–2047 (2016).
55. Chang, L.-X. et al. A 24-Gd nanocapsule with a large magnetocaloric effect. *Chem. Commun.* **49**, 1055–1057 (2013).
56. Gu, X. & Xue, D. Surface modification of high-nuclearity lanthanide clusters: two tetramers constructed by cage-shaped {Dy<sub>26</sub>} clusters and isonicotinate linkers. *Inorg. Chem.* **46**, 3212–3216 (2007).
57. Zheng, X.-Y. et al. Mixed-anion templated cage-like lanthanide clusters: Gd<sub>27</sub> and Dy<sub>27</sub>. *Inorg. Chem. Front.* **3**, 320–325 (2016).
58. Sheldrick, G. M. SHELXT – Integrated space-group and crystal-structure determination. *Acta Crystallogr. C Struct. Chem.* **71**, 3–8 (2015).

## Acknowledgements

This work was supported by the National Natural Science Foundation of China (21771043 and 21601038).

## Author contributions

Z.-L.L. and H.-L.W. contributed the crystal structure and HRESI-MS tests. Z.-H.Z., H.-H. Z., and F.-P.L. contributed the data analysis and description. T.L. and H.-F. assisted the data analysis. X.-F.M. contributed analysis of HRESI-MS and the speculation of the mechanism.

## Competing interests

The authors declare no competing interests.

## Additional information

Supplementary information is available for this paper at <https://doi.org/10.1038/s42004-020-0276-3>.

Correspondence and requests for materials should be addressed to Z.-H.Z., X.-F.M., H.-H.Z. or F.-P.L.

Reprints and permission information is available at <http://www.nature.com/reprints>

**Publisher's note** Springer Nature remains neutral with regard to jurisdictional claims in published maps and institutional affiliations.



**Open Access** This article is licensed under a Creative Commons Attribution 4.0 International License, which permits use, sharing, adaptation, distribution and reproduction in any medium or format, as long as you give appropriate credit to the original author(s) and the source, provide a link to the Creative Commons license, and indicate if changes were made. The images or other third party material in this article are included in the article's Creative Commons license, unless indicated otherwise in a credit line to the material. If material is not included in the article's Creative Commons license and your intended use is not permitted by statutory regulation or exceeds the permitted use, you will need to obtain permission directly from the copyright holder. To view a copy of this license, visit <http://creativecommons.org/licenses/by/4.0/>.

© The Author(s) 2020